Supplementary of

A combination of Time-Variable Gravity Field Solutions from Multi-Satellite Datasets (1993-2024) via Least-Squares Collocation

Lin Zhang[1], Yunzhong Shen[1], Nico Sneeuw[2], Peyman Saemian[2], Kunpu Ji[3], Qiujie Chen[1], Fengwei Wang[1],

[1] College of Surveying and Geo-informatics, Tongji University, Shanghai, China

[2] Institute of Geodesy, University of Stuttgart, Stuttgart, Germany

[3] Department of Land Surveying and Geo-Informatics, The Hong Kong Polytechnic University, Hong Kong, China

**Correspondence author:* Yunzhong Shen, E-mail: yzshen@tongji.edu.cn

A. Supplementary Tables and Figures

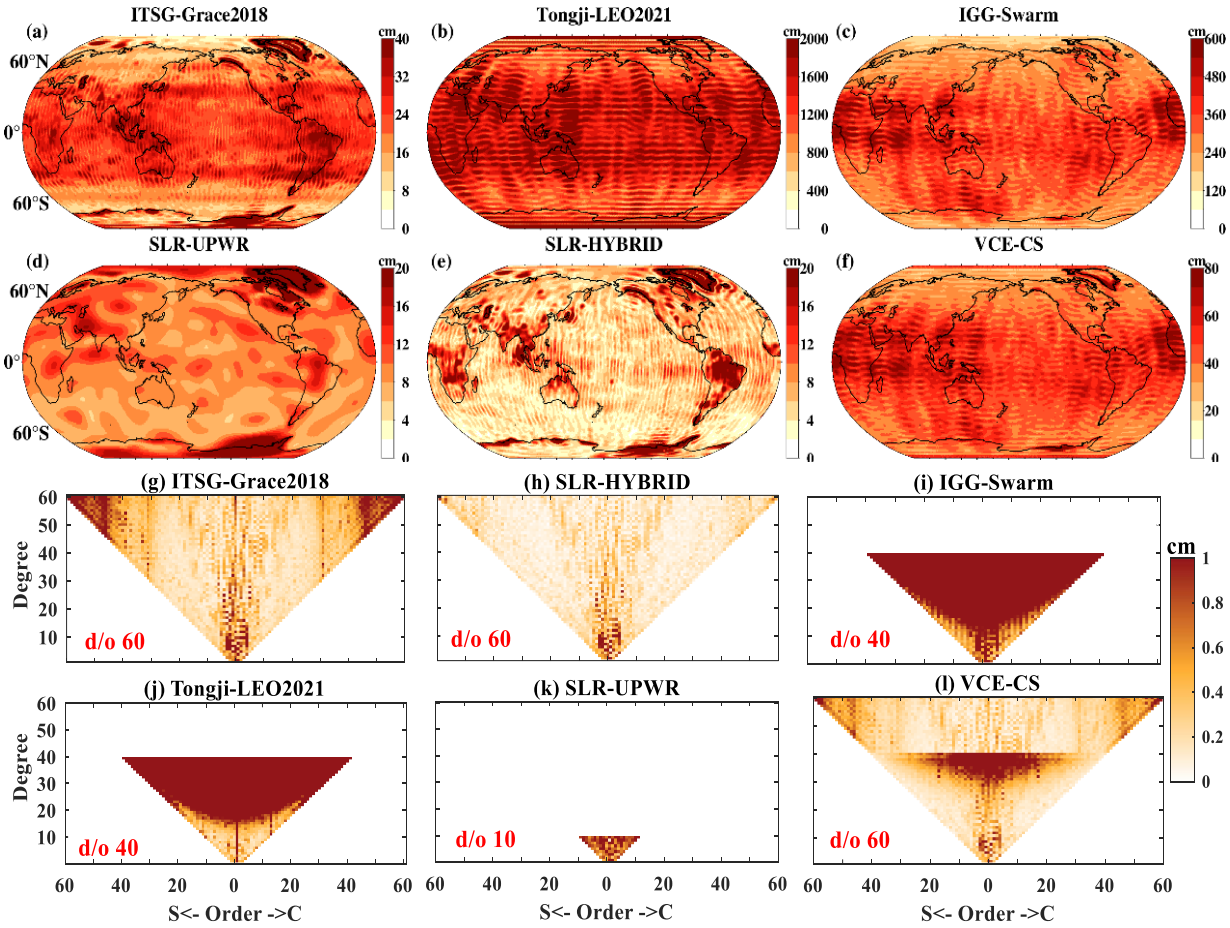

Figure S1: (a-f) RMS of spatial TWSAs and (g-l) SHCs derived from individual and VCE-CS.

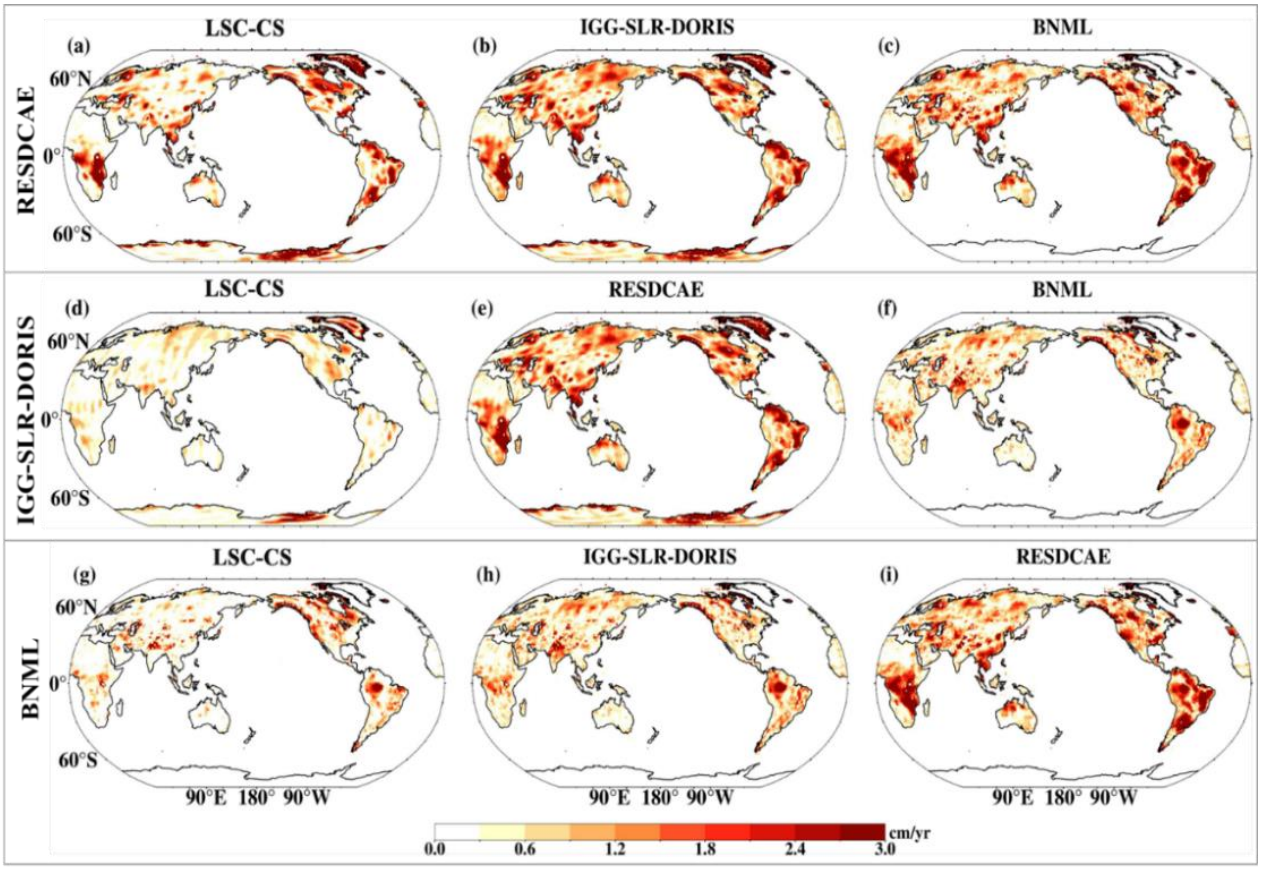

Figure S2: Linear trend differences of global TWSA derived from various solutions relative to RESDCAE, IGG-SLR-DORIS, and BNML corresponding to the first to third rows.

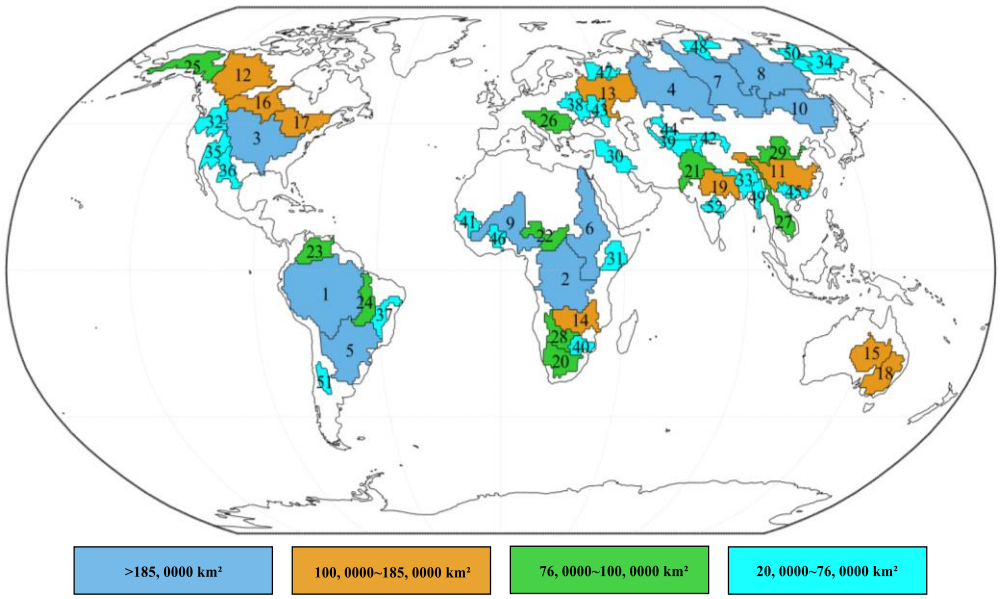

1. Amazon	2. Congo	3. Mississippi	4. Ob	5. Parana	6. Nile	7. Yenisey	8. Lena	9. Niger
10. Amur	11. Yangtze	12. Mackenzie	13. Volga	14. Zambeze	15. Lake_Eyre	16. Nelson	17. St_Lawrence	18. Murray
19. Ganges	20. Orange	21. Indus	23. Orinoco	24. Tocantins	25. Yukon	26. Danube	27. Mekong	28. Cubango
29. Yellow	30. Euphrates	31. Jubba	32. Columbia	34. Kolyma	35. Colorado	36. Rio_Grande	37.Sao_Francisco	38. Dniepr
39. Amu_Darya	40. Limpopo	41. Senegal	42. Tarim	43. Don	44. Syr_Darya	45. Xi_Hsi_Pearl	46. Volta	47. Northern
48. Khatanga	49. Irrawaddy	50. Indigirka	51. Salado	52. Godavari				

Figure S3: Spatial distributions of 52 major basins over the world, with different colors representing various area scales.

Table S1. Details of multi-type data products.

	Data type	Sources	Period	Maximum d/o (Grid resolutions)
TVGFS	GRACE/GFO	ITSG-Grace2018 [1]	2002.04-2024.12	60
	Swarm	IGG-Swarm [2]	2014.08-2021.03	40
	LEO	Tongji-LEO2021 [3]	1993.01-2004.12	
	SLR	IGG-SLR-UPWR [4]	1995.02-2023.11	10
		IGG-SLR-HYBRID [5]	1993.01-2020.12	60
Previous studies	IGG-SLR-DORIS [6]	GRACE SHCs/SLR/DORIS	1984.01-2023.12	60
	BNML [7]	NOAH/CLSM	1960.01-2022.12	1° x 1 °
	RESDCAE [8]	GRACE Mascon/SLR/ERA5	1994.01-2021.12	
	Mascon	CSR RL06 [9]	2002.04-2024.12	0.25 ° x 0.25 °
		JPL RL06 [10]		3° x 3 °
Sea level budget	$\Delta h_{\text{thermosteric}}$	[11]	1900.01-2018.12	Time series (Yearly)
	Δh_{GrIS}, Δh_{AIS}			
	GMSL	[11]		
		Satellite altimetry [12]	1993.01-2024.12	Time series (Monthly)
Water balance equation	Precipitation	CRUv4.09 [13]	1901.01-2024.12	0.5 ° x 0.5 °
		GPCCv2020 [14]	1982.01-2020.12	1 ° x 1 °
		TRMM [15]	1998.01-2020.01	0.25 ° x 0.25 °
	Evaporation	GLEAM [16]	1993.01-2024.12	0.1 ° x 0.1 °
		FluxCom [17]	2001.01-2013.12	0.5 ° x 0.5 °
		PML-v2 [18]	2002.06-2019.08	0.5 ° x 0.5 °
		Global-ET [19]	1993.01-2006.12	1 ° x 1 °
	Runoff	G-RUN [20]	1901.07-2019.12	0.5 ° x 0.5 °
		SURFEX-TRIP [21]	1979.01-2012.12	
		W3RA [22]		
		CNRDv1 [23]	2001.01-2018.12	0.25 ° x 0.25 °
Ice Sheets	AIS, GrIS	IMBIE [24]	1993.01-2020.12	Time series (Monthly)

B. Iterative process for combining TVGFS

Since the estimated equations for $\hat{\boldsymbol{x}}$ and $\hat{\boldsymbol{s}}_k$ in Eqs. (8) and (9) are mutually nested; the estimation process is iteratively conducted. This process involves updating the variance factors $\sigma_{e_i}^2$, regularization parameter α, regularization matrix $\boldsymbol{R}$, optimal variables of GM model, as summarized in Table S2.

The iteration initializes with variance factors $\left(\sigma_{e_i}^2\right)^{(0)} = 1$ for $i = 1, \ldots, q_k$, NSS $(\hat{\boldsymbol{s}}_k)^{(0)} = \boldsymbol{0}$, and parameters obtained from least-squares solutions ($(\hat{\boldsymbol{x}})^{(0)} = \hat{\boldsymbol{x}}_{ls}$).

During the first iteration, covariance matrix $\boldsymbol{\Sigma}_{e_k}^{(0)} = \left(\sigma_{e_i}^2\right)^{(0)} \boldsymbol{P}_{e_{k,i}}^{-1}$ and regularization matrix $\boldsymbol{R}^{(0)} = \left(\boldsymbol{D}\boldsymbol{T}\hat{\boldsymbol{x}}_g^{(0)}\left(\hat{\boldsymbol{x}}_g^{(0)}\right)^T\boldsymbol{T}^T\boldsymbol{D}^T\right)^{-1}$ are computed beforehand, where $\hat{\boldsymbol{x}}_g^{(0)}$ represents the spatial expression of $(\hat{\boldsymbol{x}})^{(0)}$. $\alpha^{(0)}$ is determined using the minimum MSE criterion [25; 26]. Subsequently, $(\hat{\boldsymbol{x}})^{(1)}$ is updated via Eq. (8), while $(\hat{\boldsymbol{s}}_k)^{(1)}$ is updated using bi-directional KF (Eqs. (10) and (11)), with r, τ_s, and σ_s^2 of GM process determined by minimizing Eq. (12). The variance factors $\left(\sigma_{e_{k,i}}^2\right)^{(1)}$ are updated using bias-corrected VCE [27] with $\alpha^{(0)}$, $\boldsymbol{R}^{(0)}$, and $(\hat{\boldsymbol{x}})^{(1)}$.

In the hth iteration, $\boldsymbol{\Sigma}_{e_k}^{(h)} = \left(\sigma_{e_{k,i}}^2\right)^{(h)} \boldsymbol{P}_{e_{k,i}}^{-1}$ and $\boldsymbol{R}^{(h)} = \left(\boldsymbol{DT}\hat{\boldsymbol{x}}_g^{(h)}\left(\hat{\boldsymbol{x}}_g^{(h)}\right)^T \boldsymbol{T}^T \boldsymbol{D}^T\right)^{-1}$; $\alpha^{(h)}$ is determined using the minimum MSE criterion. Subsequently, $(\hat{\boldsymbol{x}})^{(h+1)}$ is updated via Eq. (8), and $(\hat{\boldsymbol{s}}_k)^{(h+1)}$ is updated via bi-directional KF (Eqs. (10) and (11)), with r, τ_s, and σ_s^2 determined by minimizing Eq. (12). The variance factors $\left(\sigma_{e_{k,i}}^2\right)^{(h+1)}$ are updated using bias-corrected VCE with $\alpha^{(h)}$, $\boldsymbol{R}^{(h)}$, and $(\hat{\boldsymbol{x}})^{(h+1)}$.

Finally, the iteration continues until the differences of regularization solutions $\hat{\boldsymbol{x}}$ between consecutive iterations falls below 1% (i.e., $\frac{\|\hat{\boldsymbol{x}}^{(h)} - \hat{\boldsymbol{x}}^{(h-1)}\|_2}{\|\hat{\boldsymbol{x}}^{(h-1)}\|_2} < 0.01$). The combined TVGFS $\hat{\boldsymbol{y}}_k = \bar{\boldsymbol{A}}_k \hat{\boldsymbol{x}} + \hat{\boldsymbol{s}}_k$, with $\bar{\boldsymbol{A}}_k = [1 \quad \Delta t_k \quad \Delta t_k^2 \quad \sin(2\pi\Delta t_k) \quad \cos(2\pi\Delta t_k) \quad \sin(4\pi\Delta t_k) \quad \cos(4\pi\Delta t_k)] \otimes \boldsymbol{I}_M$.

Table S2. Pseudocode for iteratively combining TVGFS

The flowchart of fusing time-variable gravity field models
Input:
$\boldsymbol{y}_{k,i}$ and $\boldsymbol{P}_{e_{k,i}}$ for ith institution
initial $\left(\sigma_{e_{k,i}}^2\right)^{(0)} = 1$, $(\hat{\boldsymbol{s}}_k)^{(0)} = \boldsymbol{0}$, $(\hat{\boldsymbol{x}})^{(0)} = \hat{\boldsymbol{x}}_{ls}$,
iteration threshold $\delta = 0.01$
Output:
Combined parameters $\hat{\boldsymbol{x}}$
Combined NSS $\hat{\boldsymbol{s}}_k$
Begin
$\boldsymbol{\Sigma}_{e_{k,i}}^{(0)} = \left(\sigma_{e_{k,i}}^2\right)^{(0)} \boldsymbol{P}_{e_{k,i}}^{-1}$ and $\boldsymbol{R}^{(0)} = \left(\boldsymbol{DT}\hat{\boldsymbol{x}}_g^{(0)}\left(\hat{\boldsymbol{x}}_g^{(0)}\right)^T \boldsymbol{T}^T \boldsymbol{D}^T\right)^{-1}$;
Determine $\alpha^{(0)}$ on the minimum MSE [25; 26];
Update $\hat{\boldsymbol{x}}^{(1)}$ using Eq. (8);
Update $\hat{\boldsymbol{s}}_k^{(1)}$ using Eqs. (10) and (11) with r, τ_s, and σ_s^2 of GM model determined by Eq. (12);
Update $\left(\sigma_{e_{k,i}}^2\right)^{(1)}$ using bias-corrected VCE [27] with $\alpha^{(0)}$, $\boldsymbol{R}^{(0)}$, $\hat{\boldsymbol{x}}^{(1)}$
$h = 1$;
while true **do**
$\boldsymbol{\Sigma}_{e_{k,i}}^{(h)} = \left(\sigma_{e_{k,i}}^2\right)^{(h)} \boldsymbol{P}_{e_{k,i}}^{-1}$ and $\boldsymbol{R}^{(h)} = \left(\boldsymbol{DT}\hat{\boldsymbol{x}}_g^{(h)}\left(\hat{\boldsymbol{x}}_g^{(h)}\right)^T \boldsymbol{T}^T \boldsymbol{D}^T\right)^{-1}$;
Update $\alpha^{(h)}$ based on the minimum MSE;
Update $\hat{\boldsymbol{x}}^{(h+1)}$ using Eq. (8);
Update $\hat{\boldsymbol{s}}_k^{(h+1)}$ using Eqs. (10) and (11) with r, τ_s, and σ_s^2 of GM model determined by Eq. (12);
Update $\left(\sigma_{e_{k,i}}^2\right)^{(h+1)}$ using bias-corrected VCE with $\alpha^{(h)}$, $\boldsymbol{R}^{(h)}$, $\hat{\boldsymbol{x}}^{(h+1)}$
if $\frac{\|\hat{\boldsymbol{x}}^{(h+1)} - \hat{\boldsymbol{x}}^{(h)}\|_2}{\|\hat{\boldsymbol{x}}^{(h)}\|_2} < \delta$ **then**
break;
else
$h = h + 1$;
end if
end while
$\hat{\boldsymbol{x}} = \hat{\boldsymbol{x}}^{(h+1)}$; $\hat{\boldsymbol{s}}_k = \hat{\boldsymbol{s}}_k^{(h+1)}$;
End

C. Evaluation Metrics

(1) Sea level budget

TWS contribution to global mean sea level (Δh_{GMSL}) variations is deived by subtracting thermosteric expansion ($\Delta h_{\mathrm{therm}}$) and mass changes of Greenland (Δh_{GrIS}) and Antarctic (Δh_{AIS}) Ice Sheets from total GMSL [11],

$$\Delta h_{\mathrm{TWS}} = \Delta h_{\mathrm{GMSL}} - \Delta h_{\mathrm{therm}} - \Delta h_{\mathrm{GrIS}} - \Delta h_{\mathrm{AIS}} \tag{S1}$$

(2) Water balance equation

TWSCs from TVGFS ($\Delta\mathrm{TWSC}_{\mathrm{TVGFS}}$) computed from TWSAs between two adjacent months can be evaluated by computing the misclosure with water balance estimates composed of precipitation (P), runoff (R), and evaporation (E) [28],

$$\Delta\mathrm{TWSC}_{\mathrm{TVGFS}} = \mathrm{P} - \mathrm{R} - \mathrm{E} \tag{S2}$$

(3) Land-to-ocean Signal-to-Noise Ratios (SNRs)

The SNR at latitude θ_i (i.e., SNR_{θ_i}) is computed using the Root Mean Square (RMS) of mass changes over land ($\mathrm{MASS}_{\mathrm{land},\theta_i}$) and ocean ($\mathrm{MASS}_{\mathrm{ocean},\theta_i}$) at the corresponding latitude[29;30],

$$\mathrm{SNR}_{\theta_i} = \frac{\mathrm{RMS}\left(\mathrm{MASS}_{\mathrm{land},\theta_i} + \mathrm{Err}_{\theta_i}\right)}{\mathrm{RMS}\left(\mathrm{MASS}_{\mathrm{ocean},\theta_i} + \mathrm{Err}_{\theta_i}\right)} \tag{S3}$$

The overall SNR is determined using the global latitude weighted average, $\mathrm{SNR} = \frac{\sum_{i=1}^{n} \cos\theta_i \cdot \mathrm{SNR}_{\theta_i}}{\sum_{i=1}^{n} \cos\theta_i}$; n indicates the number of latitude divisions in the global grid.

(4) Degree Power σ_l^2

$$\sigma_l^2 = \frac{\sum_{m=0}^{l}\left[\left(\Delta C_{lm}^{\gamma}\right)^2 + \left(\Delta S_{lm}^{\gamma}\right)^2\right]}{2l+1} \tag{S4}$$

where, C_{lm}^{γ} and ΔS_{lm}^{γ} are filtered SHCs at degree l and order m[31].

(5) Nash-Sutcliffe Efficiency (NSE)

$$\mathrm{NSE} = 1 - \frac{\sum_{\mathrm{t}=1}^{\mathrm{n}}(\mathrm{TWSA}_{\mathrm{evaluated}}(\mathrm{t}) - \mathrm{TWSA}_{\mathrm{reference}}(\mathrm{t}))^2}{\sum_{\mathrm{t}=1}^{\mathrm{n}}(\mathrm{TWSA}_{\mathrm{evaluated}}(\mathrm{t}) - \overline{\mathrm{TWSA}_{\mathrm{reference}}})^2} \tag{S5}$$

where, TWSA derived from various solutions to be evaluated and the references are denoted as $\mathrm{TWSA}_{\mathrm{filtered}}$ and $\mathrm{TWSA}_{\mathrm{reference}}$; $\overline{\mathrm{TWSA}_{\mathrm{reference}}}$ is the mean value of $\mathrm{TWSA}_{\mathrm{reference}}$. NSE approaching 1 means excellent consistency while negative NSE denotes worse consistency[32].

References

[1] Kvas, A., Behzadpour, S., Ellmer, M., et al. (2019). ITSG-Grace2018: Overview and Evaluation of a New GRACE-Only Gravity Field Time Series. Journal of Geophysical Research-Solid Earth, 124(8), 9332-9344. DOI:

10.1029/2019jb017415.

[2] Lück, C., Kusche, J., Rietbroek, R., et al. (2021). IGG-Swarm: Temporal Gravity Models from Swarm. GFZ Data Services. DOI: 10.5880/icgem.2021.002.

[3] Chen, Q., Wang, F., Shen, Y., et al. (2022). Monthly gravity field solutions from early LEO satellites' observations contribute to global ocean mass change estimates over 1993～2004. Geophysical Research Letters, 49, e2022GL099917. DOI: 10.1029/2022GL099917.

[4] Gałdyn, F., Sośnica, K., Zajdel, R., et al. (2024). Long-term ice mass changes in Greenland and Antarctica derived from satellite laser ranging. Remote Sensing of Environment, 302, 113994. DOI: 10.1016/j.rse.2024.113994.

[5] Locher, A., & Kusche, J. (2021). A hybrid approach for recovering high-resolution temporal gravity fields from satellite laser ranging. J. Geod. 95, 6. DOI: 10.1007/s00190-020-01460-x.

[6] Löcher, A., Kusche, J., & Nie, Y. (2025). A 40-year record of the Earth's time-variable gravity field from SLR and DORIS. Advances in Space Research. DOI: 10.1016/j.asr.2025.05.089.

[7] Mandal, N., Das, P., & Chanda, K. (2025). Machine-learning-based reconstruction of long-term global terrestrial water storage anomalies from observed, satellite and land-surface model data. Earth System Science Data, 17(6), 2575-2604. DOI: 10.5194/essd-17-2575-2025.

[8] Uz, M., Akyılmaz, O., Shum, C. K., et al. (2024). High-resolution temporal gravity field data products: Monthly mass grids and spherical harmonics from 1994 to 2021. Scientific Data, 11(1), 71. DOI: 10.1038/s41597-023-02887-5.

[9] Save, H., Bettadpur, S., & Tapley, B. D. (2016). High-resolution CSR GRACE RL05 mascons. Journal of Geophysical Research: Solid Earth, 121(10), 7547-7569. DOI: 10.1002/2016jb013007.

[10] Watkins, M. M., Wiese, D. N., Yuan, D. N., et al. (2015). Improved methods for observing Earth's time variable mass distribution with GRACE using spherical cap mascons. Journal of Geophysical Research: Solid Earth, 120(4), 2648-2671. DOI: 10.1002/2014jb011547.

[11] Frederikse, T., Landerer, F., Caron, L., et al. (2020). The causes of sea-level rise since 1900. Nature, 584(7821), 393-397. DOI: 10.1038/s41586-020-2591-3.

[12] Beckley, B., Yang, X., Zelensky, N. P., et al. (2025). Global Mean Sea Level Trend from Integrated Multi-Mission Ocean Altimeters TOPEX/Poseidon, Jason-1, OSTM/Jason-2, Jason-3, and Sentinel-6 Version 5.2. Ver. 5.2. PO. DAAC, CA, USA. DOI: 10.5067/GMSLM-TJ152.

[13] Harris, I., Osborn, T. J., Jones, P., et al. (2020). Version 4 of the CRU TS monthly high-resolution gridded multivariate climate dataset. Scientific data, 7(1), 109. DOI: 10.1038/s41597-020-0453-3.

[14] Schneider, U., Becker, A., Finger, P., et al. (2011). GPCC Full Data Reanalysis Version 6.0 at 0.5°: Monthly Land-Surface Precipitation from Rain-Gauges built on GTS-based and Historic Data. DOI: 10.5676/DWD_GPCC/FD_M_V7_050.

[15] Mission, T. R. M. (2011). TRMM (TMPA/3B43) Rainfall Estimate L3 1 month 0.25 degree x 0.25 degree V7, Greenbelt, MD, Goddard Earth Sciences Data and Information Services Center (GES DISC). Retrieved from January, 11, 2019. DOI: 10.5067/TRMM/TMPA/MONTH/7.

[16] Miralles, D. G., Bonte, O., Koppa, A., et al. (2025). GLEAM4: global land evaporation and soil moisture dataset at 0.1 resolution from 1980 to near present. Scientific data, 12(1), 416. DOI: 10.5281/zenodo.14056079.

[17] Jung, M., Koirala, S., Weber, U., et al. (2019). The FLUXCOM ensemble of global land-atmosphere energy fluxes. Scientific data, 6(1), 74. DOI: 10.1038/s41597-019-0076-8.

[18] Zhang, Y., Kong, D., Gan, R., et al. (2019). Coupled estimation of 500 m and 8-day resolution global evapotranspiration and gross primary production in 2002–2017. Remote sensing of environment, 222, 165-182. DOI: 10.1016/j.rse.2018.12.031.

[19] Zhang, K., Kimball, J. S., Nemani, R. R., et al. (2010). A continuous satellite-derived global record of land surface evapotranspiration from 1983 to 2006. Water Resources Research, 46(9). DOI: 10.1029/2009WR008800.

[20] Ghiggi, G., Humphrey, V., Seneviratne, S. I., et al. (2021). G-RUN ENSEMBLE: A multi-forcing observation-based global runoff reanalysis. Water Resources Research, 57(5), e2020WR028787. DOI: 10.1029/2020WR028787.

[21] Decharme, B., Martin, E., & Faroux, S. (2013). Reconciling soil thermal and hydrological lower boundary conditions in

land surface models. Journal of Geophysical Research: Atmospheres, 118(14), 7819-7834. DOI: 10.1002/jgrd.50631.

[22] Van Dijk, A. I. J. M., & Warren, G. (2010). The Australian water resources assessment system. Version 0.5, 3(5). DOI: 10.4225/08/5852dd9bb578c.

[23] Gou, J., Miao, C., Samaniego, L., et al. (2021). CNRD v1. 0: a high-quality natural runoff dataset for hydrological and climate studies in China. Bulletin of the American Meteorological Society, 102(5), E929-E947. DOI: 10.1175/BAMS-D-20-0094.1.

[24] Shepherd, A., Ivins, E., Rignot, E., et al. (2021). Antarctic and Greenland ice sheet mass balance 1992-2020 for IPCC AR6 (version 1.0). UK Polar Data Centre, Natural Environment Research Council, UK Research & Innovation [data set]. DOI: 10.5285/77b64c55-7166-4a06-9def-2e400398e452.

[25] Shen, Y., Xu, P., & Li, B. (2012). Bias-corrected regularized solution to inverse ill-posed models. Journal of Geodesy, 86(8), 597-608. DOI: 10.1007/s00190-012-0542-y.

[26] Ji, K., Shen, Y., Chen, Q., et al. (2022). An Adaptive Regularized Solution to Inverse Ill-Posed Models. IEEE Transactions on Geoscience and Remote Sensing, 60, 15. DOI: 10.1109/tgrs.2022.3205572.

[27] Xu, P., Shen, Y., Fukuda, Y., et al. (2006). Variance component estimation in linear inverse ill-posed models. Journal of Geodesy, 80(2), 69-81. DOI: 10.1007/s00190-006-0032-1.

[28] Zhang, L., Shen, Y., Chen, Q., et al. (2023). Influence factors and mechanisms of 2015–2016 extreme flood in Pearl River Basin based on the WSDI from GRACE. Journal of Hydrology: Regional Studies, 47, 101376. DOI: 10.1016/j.ejrh.2023.101376.

[29] Chen, J. L., Wilson, C. R., Tapley, B. D., et al. (2017). Long-term and seasonal Caspian Sea level change from satellite gravity and altimeter measurements. Journal of Geophysical Research: Solid Earth, 122(3), 2274-2290. DOI: 10.1002/2016JB013595.

[30] Kusche, J. (2007). Approximate decorrelation and non-isotropic smoothing of time-variable GRACE-type gravity field models. Journal of Geodesy, 81(11), 733-749.

[31] Zhang, L., Shen, Y., Ji, K., et al. (2025). An Enhanced Parameter Filtering Approach for Postprocessing GRACE Monthly Gravity Field Models. IEEE Geoscience and Remote Sensing Letters. DOI: 10.1109/LGRS.2025.3575197

[32] Werth, S., Güntner, A., Schmidt, R., et al. (2009). Evaluation of GRACE filter tools from a hydrological perspective. Geophysical Journal International, 179(3), 1499-1515. DOI: 10.1111/j.1365-246X.2009.04355.x.